Available online at www.sciencedirect.com

SciVerse ScienceDirect

journal homepage: www.elsevier.com/locate/he

Review

Turbulent non-premixed hydrogen-air flame structure in the pressure range of 1–10 atm

F. Tabet [a,*], B. Sarh [b,c], I. Gökalp [b]

[a] European Institute for Energy Research (EIFER) – EDF R&D, Emmy-Noether-Strasse 11, D-76131 Karlsruhe, Germany
[b] Institut de Combustion, Aérothermique, Réactivité et Environnement (ICARE), Centre National de la Recherche Scientifique (CNRS), 1C avenue de la recherché scientifique, Orléans 45071 Cedex 2, France
[c] Institut Universitaire de Technologie d'Orléans (IUT-Orléans), Université d'Orléans, 16 Rue d'Issoudun, BP. 16729, 45067 Orléans Cedex 2, France

ARTICLE INFO

Article history:
Received 11 February 2011
Received in revised form
19 August 2011
Accepted 19 August 2011
Available online 1 October 2011

Keywords:
Mixing
Pressure
Diffusion flame
Flame structure
Flamelet approach
Radiation

ABSTRACT

A numerical study of hydrogen turbulent diffusion flame structure is carried out in the pressure range of 1–10 atm with a special emphasis on mixing. The investigation is conducted under constant volumetric fuel and air flows. Mixing is characterized by mixture fraction, its variance and the scalar dissipation rate. The flow field and the chemistry are coupled by the flamelet assumption. Mixture fraction and its variance are transported by computational fluid dynamic (CFD). Computational predictions are analysed at two radial stations (the first one represent the near-field region and the second one the far-field region). The computational results indicate a deterioration of mixing with pressure rise. As a result, flame reaction zone becomes thicker. In addition, mixing and flame structure sensitivity to pressure are found to be high in the first location. Further analysis revealed that the gas becomes increasingly heavy with pressure rise, which hampered its ability to mix.

1. Introduction

Hydrogen-rich alternative fuels such as syngas are expected to serve as a clean energy in power generation systems [1]. The combustion of these blended fuels is an important component of the IGCC (Integrated Gasification Combined Cycle) concept. Indeed, the emergence of this technology for incorporating carbon capture in coal-based power plants increases the need for gas turbine combustors to operate on a range of hydrogen-rich fuels produced by gasification. Existing lean premixed gas turbines are susceptible to a number of problems including flame flashback and combustion instabilities when operating on fuels containing large amounts of hydrogen [2]. Combustion strategies for syngas and hydrogen utilize diffusion flames where the fuel and air are not premixed prior to combustion [3]. The challenge is to design a diffusion flame combustor that meets NO_x regulation goals. Staged combustion, lean direct injection, and highly strained diffusion flame combustors seems to be a promising technologies for that purpose [4].

* *Corresponding author*. Tel.: +49 (0) 721 6105 1332; fax: +49 (0) 721 6105 1483.
E-mail address: tabet@eifer.org (F. Tabet).
0360-3199/$ – see front matter
doi:10.1016/j.ijhydene.2011.08.064

Nomenclature

C_P	Specific heat coefficient at pressure constant, $J \cdot kg^{-1} \cdot K^{-1}$
D	Diameter of the burner, m
Fr	Froude number
frac	Fractional temperature
g	Earth gravitation, $m^2 \cdot s^{-1}$
H	Enthalpy, $J \cdot kg^{-1}$
h°	Enthalpy of formation, $J \cdot kg^{-1}$
I	radiation intensity, $W\ m^{-2} \cdot sr^{-1}$
k	Turbulent kinetic energy, $m^2 \cdot s^{-2}$
Le	Lewis number
$\dot{m}$	Mass flow, $kg \cdot s^{-1}$
MW	Molecular weight, $g \cdot mol^{-1}$
P	Pressure, Pa
Pr	Prandtl number
r	Radial direction, m
R	Universal gas constant, $J \cdot kg^{-1} \cdot K^{-1}$
Sc	Schmidt number
T	Temperature, K
U	Mean velocity, $m \cdot s^{-1}$
u_i	velocity components (u and v in axisymmetric configuration), $m \cdot s^{-1}$
x	Axial direction, m
Y	Mass fraction
Z	Mixture fraction

Greek letters

ε	Dissipation rate of turbulent kinetic energy, $m^2 \cdot s^{-3}$
μ	Dynamic viscosity, $kg \cdot m^{-1} \cdot s^{-1}$
ϕ	Global equivalence ratio
ρ	Density, $kg \cdot m^{-3}$
χ	Scalar dissipation rate, s^{-1}
σ	Steffan-Boltzmann constant, $5.669 \times 10^{-8}\ W \cdot m^{-2} \cdot K^{-4}$,
α	Absorption coefficient, m^{-1}

Subscripts

c	Air stream, co-flow
cent	Centerline
J	Fuel stream
F	Fuel
f	Flame
g	Gas, burnt gas
n	Species
O	Oxidizer, Air
ref	Reference
st	Stoichiometric
t	turbulent
½	Half width
0	Injection section

Superscripts

~	Favre-averaged
-	Reynolds-averaged
"	Fluctuations

Abbreviations

TNF	Turbulent Non-premixed Flames
SLFM	Steady Laminar Flamelet Model
PDF	Probability Density Function

Fuels containing large amounts of hydrogen have combustion properties highly depending on composition, in particular hydrogen concentration, and operating conditions such as pressure [5]. Prior to analyse the impact of the variability in the alternative fuel composition and heating value on combustion performance and emissions, it is important to well identify the behaviour of hydrogen diffusion flames at high pressure. This study is carried out in this context, where the characteristics (flame length and width, radiation, mixing) of hydrogen diffusion flames are investigated at high pressure (up to 10 atm).

Research activities on hydrogen diffusion flames at pressures above atmospheric in open literature are often conducted using counter-flow configuration both experimentally and theoretically. A thorough understanding of strained laminar flames is a prerequisite to achieve improved knowledge of more complex system. The literature on counter-flow H_2/O_2 diffusion flames is abundant. The purpose of these studies is, in general, to analyse the influence of main parameters such as dilution (with CO_2 or N_2), preheating, operating pressure and radiation on the flame structure [6]. A recent paper [7] has summarized various existing numerical studies in this subject area. Concerning pressure effect, early works focussed on the relationship between operating pressure and extinction limits in both H_2/O_2 and H_2/air diffusion flames [8,9]. Recent studies are more dedicated to the characterization of a relationship between the flame thickness and heat release rate function of operating pressure and strain rate [7].

In spite of the many research studies performed on counter-flow configuration, few literatures exists on hydrogen jet flames at elevated pressures. The studies available are mainly related to fire hazard of a rapid leakage of compressed hydrogen in order to develop a scientific basis for evaluating credible safety scenarios and to provide technical data for hydrogen codes and standards' decisions [10–13].

Recently, a couple of investigations have been carried out on hydrogen jet flames in gas turbine conditions. The main reason for the growing interest in this topic is due to the development of a fuel flexible (syngas and hydrogen fuels) advanced gas turbine for IGCC. These works are usually performed in the framework of a research program initiated by gas turbine manufacturers [3,14,15] to evaluate the reliability of the components including the burner designed for natural gas operation.

Although the above survey manifests substantial efforts that have been devoted to investigate hydrogen diffusion flames characteristics, a comprehensive understanding of these flames structures at different operating pressure has not been yet consummated. This paper presents a CFD simulation of the structure of turbulent hydrogen jet flame in air co-flow at different operating pressure (up to 10 atm). The interest is

focused on mixing as the near-field region of this flame is characterized by strong gradients of velocity and density. The analysis is conducted in the configuration of Barlow and Carter [16]. This study complements the research work reported in Ref. [17] in which the structure of hydrogen-air turbulent non-premixed flame was examined at atmospheric pressure. A review of the most important studies at atmospheric pressure on this flame configuration is also provided in Ref. [17].

The article consists of five sections. Following a brief explanation of the flame configuration, the modelling approach is introduced. A general description of the computational method is then presented. The numerical simulation results are presented with a discussion in the last section. The conclusion summarizes the findings of the present work.

2. Flame configuration

The test case is completely described on the TNF website [18]. A central fuel jet consisting of 100% hydrogen with an inner diameter of 3.75 mm and outer diameter of 4.8 mm is surrounded by a co-flow air stream (Fig. 1). The co-flowing air velocity was fixed at 1 $m \cdot s^{-1}$. The mean inlet velocity of the fuel jet was 296 $m \cdot s^{-1}$ and the Reynolds number of the flame was 10,000. The flame had a visible length of 675 mm. The experiments were carried out by Barlow and Carter [16] for the temperature and species concentrations and by Flury and Schlatter [19] for the flow field. Experimental data are available in Ref. [18]. A summary of the flame characteristics are reported in Table 1, where m and R_ρ are the velocity and density ratios at the injection location ($m = U_c/U_J$ and $R_\rho = \rho_c/\rho_J$). The Reynolds number of the flame was selected such that the flame was fully turbulent without effects of buoyancy (the Froude number at the injection section is around 17000) and local extinction. The flame was attached and was in a fully burning regime and may therefore be considered to be a typical case which falls within the flamelet regime.

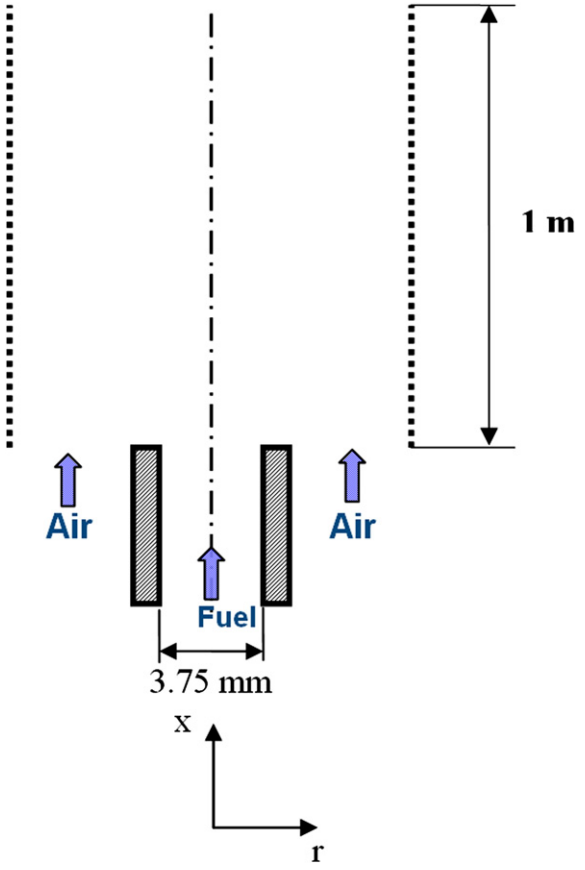

Fig. 1 – Flame configuration.

The experimental data showed deviations from chemical equilibrium near the fuel nozzle (the super-equilibrium values are about six times higher at the locations close to the burner) and the OH zone is much broader than at equilibrium. Also, there is a decay of the OH super-equilibrium values along the flame length approaching chemical equilibrium at the flame tip [18].

3. Modelling approach

3.1. *Turbulence model*

The steady Reynolds-averaged Navier–Stokes (RANS) equations are applied. Favre averages are used to account for variable-density effects. Turbulence is modelled by the k-ε model. The Pope correction [20] for round jets is added to the turbulence dissipation rate, ε, equation in order to improve the prediction of the spreading rate of the jet. This correction enables to keep the original coefficients of this model ($C\varepsilon_1$ and $C\varepsilon_2$). Buoyancy contributions are also considered in the turbulent dissipation rate equation.

3.2. *Chemistry model*

The flamelet model used in this study was developed by Pitsch and Peters [21]. In this formulation mixture fraction variable Z is obtained from the solution of a conservation equation with an arbitrary diffusion coefficient and appropriate boundary conditions. Note that the instantaneous thermo-chemical state of the fluid is related to mixture fraction as [22]:

$$Z = \frac{\frac{\phi Y_F}{Y_{F,0}} - \frac{Y_O}{Y_{O,0}} + 1}{\phi + 1} \tag{1}$$

where ϕ is the equivalence ratio defined by:

$$\phi = \frac{Y_{F,0}}{Y_{O,0}} \Big/ \left.\frac{Y_F}{Y_O}\right|_{st} \tag{2}$$

Mixture fraction takes values between 0 and 1 ($Z = 1$ in the fuel side and $Z = 0$ in the oxidizer side). In the above equations,

Table 1 – Flame characteristics.

Flames configurations	U_J [$m \cdot s^{-1}$]	U_c [$m \cdot s^{-1}$]	ρ_J [$Kg \cdot m^{-3}$]	m	R_ρ
H_2/Air	296	1	0.082	0.0034	15

Y_F denotes the mass fraction of fuel and Y_O the mass fraction of oxidizer.

The flame front is located at [22]:

$$Z = Z_{st} = \frac{1}{1+\phi} \tag{3}$$

Using this transport equation of mixture fraction, the flamelet equations are derived without any assumptions about the Lewis numbers for chemical species [21].

The flamelet equations are solved until steady state is achieved in pre-processing assuming $Le_n = 1$ for all the species with two input parameters which are mixture fraction (Z) and the stoichiometric scalar dissipation rate (χ_{st}). With this approach, the functional dependence of the scalar dissipation rate on mixture fraction $\chi(Z)$ is parameterized by χ_{st}. This value acts as an external parameter that is imposed on the flamelet structure by the mixture fraction field. A set of discrete values of χ_{st} are used from equilibrium ($\chi_{st} = 0$) to a quenching value ($\chi_{st} = \chi_q$). Each flamelet is calculated using the kinetic of Yetter et *al.* [23] which contains 10 chemical species and 21 reactions. This chemical mechanism was usefully validated over a wide range of operating conditions for syngas-air mixtures [24]. The calculations were performed with AURORA tool of the CHEMKIN release 3.7 [25], software package. The conditions investigated included various parameters such as temperature (500 K $< T <$ 1500 K), pressure (1.1 and 15 atm) and composition (% of CO in the mixture). The numerical results were compared with experimental data found in the literature. It has been noted that Yetter et *al.* [23] mechanism predicts the experimental data accurately for temperatures above 1000 K, regardless of the pressure. Below 1000 K, this kinetic model predict an ignition delay time much higher than the experimental data.

The flamelet species profiles are assumed to be unaffected by heat gain/loss to the system [26] and adiabatic mass fractions are generated. Also, the effect of heat loss on the extinction limits is not taken into account. This simplification is expected to have a minor influence on this flame as reported in Ref. [27]. Therefore, the radiation term is omitted in the solution of flamelet equations.

The temperature field in non-adiabatic conditions is then obtained iteratively from enthalpy (Eq. (4) below) for a range of values of mean enthalpy gain/loss $\tilde{H}$ [27]:

$$\tilde{H} = \sum_n \tilde{Y}_n \tilde{H}_n \tag{4}$$

and:

$$\tilde{H}_n = \int_{T_{ref,n}}^{T} c_{p,n} dT + h_n^{\circ}(T_{ref,n}) \tag{5}$$

where $c_{p,n}$ is the specific heat coefficient at constant pressure. It is assumed to be function of temperature and composition and $h_n^{\circ}(T_{ref,n})$ is the formation enthalpy of species n at the reference temperature$T_{ref,n}$.

Note that multiple scalar dissipation rates which vary from near equilibrium to near extinction limit have been considered per each enthalpy gain/loss when evaluating temperature field.

The whole picture of the turbulent flame is given by averaging the laminar profiles. Statistical independence of Z and χ is assumed and the fluctuations of the scalar dissipation rate are ignored [22]. The Favre PDF required for mixture fraction is presumed to be a β-function. This PDF is controlled by its first two moments: mean mixture fraction and its variance.

The stationary solution is then stored in tables containing the profiles of density, temperature and mass fractions for all chemical species as function of mixture fraction, its variance and the stoichiometric scalar dissipation rate. The mean density is calculated from the ideal gas law:

$$\frac{1}{\overline{\rho}} = \frac{R\overline{T}}{\overline{p}} \sum_n \left(\tilde{Y}_n / MW_n\right) \tag{6}$$

In this equation $\overline{P}$ is the mean pressure, R the universal gas constant and MW_n the molar mass of species n.

Accordingly, the mean temperature and density have an extra dimension of mean enthalpy as follows [22]:

$$\tilde{T}\left(\tilde{Z}, \tilde{Z}''^2, \tilde{H}, \tilde{\chi}_{st}\right) \tag{7}$$

$$\tilde{Y}_n\left(\tilde{Z}, \tilde{Z}''^2, \tilde{\chi}_{st}\right) \tag{8}$$

$$\overline{\rho}\left(\tilde{Z}, \tilde{Z}''^2, \tilde{H}, \tilde{\chi}_{st}\right) \tag{9}$$

The coupling of chemistry and flow field is performed via the mixture fraction, its variance, the stoichiometric scalar dissipation rate and enthalpy, which are provided from the flow field calculations. The values of these parameters at each computational cell are used to extract mean scalar properties from the chemistry lookup tables. The flow field properties are updated and iterations continue until convergence criteria are met. Indeed, in the CFD code transport equations are solved for the mixture fraction and its variance. These equations are closed assuming a gradient diffusion hypothesis (first order closure) for the turbulent scalar fluxes [22]:

$$\frac{\partial}{\partial t}\left(\overline{\rho}\tilde{Z}\right) + \frac{\partial}{\partial x_i}\left(\overline{\rho}\tilde{u}_i\tilde{Z}\right) = \frac{\partial}{\partial x_i}\left(\frac{\mu_t}{Sc_t}\frac{\partial \tilde{Z}}{\partial x_i}\right) \tag{10}$$

$$\frac{\partial}{\partial t}\left(\overline{\rho}\tilde{Z}''^2\right) + \frac{\partial}{\partial x_i}\left(\overline{\rho}\tilde{u}_i\tilde{Z}''^2\right) = \frac{\partial}{\partial x_i}\left(\frac{\mu_t}{Sc_t}\frac{\partial \tilde{Z}''^2}{\partial x_i}\right) + C_g\mu_t\frac{\partial \tilde{Z}}{\partial x_i}\frac{\partial \tilde{Z}}{\partial x_i} - \overline{\rho}\tilde{\chi} \tag{11}$$

where Sc_t is the turbulent Schmidt number (it takes a value of 0.85). The constant C_g takes a value of 2.86. $\tilde{\chi}$ is the mean scalar dissipation rate, where its modelling is based on proportionality of mechanical and scalar time scales [28]:

$$\tilde{\chi} = C_d\frac{\varepsilon}{\tilde{k}}\tilde{Z}''^2 \tag{12}$$

where $C_d = 2.0$ according to Ref. [22].

3.3. *Energy equation*

A transport equation for the mean enthalpy $\tilde{H}$ is solved with the radiation source term [22]:

$$\frac{\partial}{\partial t}\left(\overline{\rho}\tilde{H}\right) + \frac{\partial}{\partial x_i}\left(\overline{\rho}\tilde{u}_i\tilde{H}\right) = \frac{\partial}{\partial x_i}\left(\frac{\mu_t}{Pr_t}\frac{\partial \tilde{H}}{\partial x_i}\right) + S_h \tag{13}$$

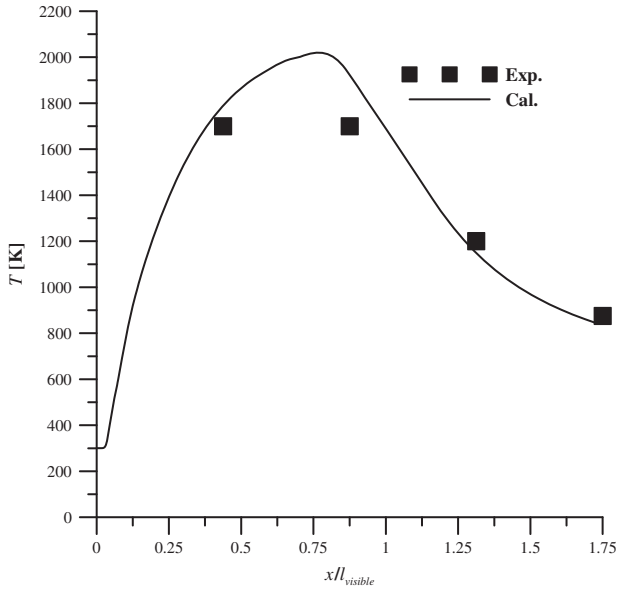

Fig. 2 – Centerline temperature distribution for H_2-Air jet flame (flame of schefer et al. [11] at 100 s).

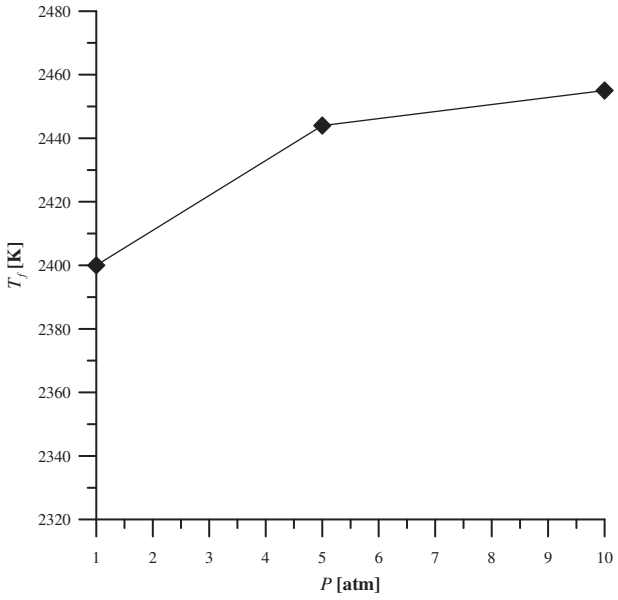

Fig. 3 – Adiabatic flame temperature.

With Pr_t the turbulent Prandtl number (it takes a value of 0.85) and S_h the source term due to radiation.

3.4. *Radiation model*

Radiation is accounted for in energy Eq. (13) by the DO (Discrete Ordinate) model in which the RTE (Radiative Transfer Equation) is solved for a finite number of discrete solid angles [29]. The heat source by radiation is given by:

$$S_h = \alpha\left(\int_{4\pi} I(r,\Omega)d\Omega - \sigma T^4\right) \quad (14)$$

where $I(r,\Omega)$ is the radiation intensity, which is a function of position and direction. α and σ are the absorption coefficient and the Stephan Boltzman constant respectively. The absorption coefficient is calculated as recommended in Ref. [30], i.e. using the curve fits for the Plank mean absorption coefficient of H_2O.

Table 2 – Operating conditions.

Constant volumetric fuel and air flows			
P [atm]	1	5	10
T_j [K]	300	300	300
U_j [m·s^{-1}]	296	296	296
ρ_j [Kg·m^{-3}]	0.082	0.41	0.82
$\dot{m}_j$ [Kg·s^{-1}]	0.268×10^{-4}	1.34×10^{-4}	2.68×10^{-4}
υ_j [m^2·s^{-1}]	1.097×10^{-4}	2.194×10^{-5}	1.097×10^{-5}
Re_j	10,000	50,000	100,000
T_c [K]	300	300	300
ρ_c [Kg·m^{-3}]	1.22	6.1	12.2
U_c [m·s^{-1}]	1	1	1
MR	87,616	87,616	87,616
Z_{st}	0.028	0.028	0.028

4. Computational details

4.1. *Description of the SLFM library*

A flamelet library is constructed for each operating pressure (1, 5 and 10 atm) with 12 values of the stoichiometric scalar dissipation rate ranging from a low value close to equilibrium to a large value close to extinction before executing the Fluent code. In each library, mean values of species mass fractions are computed for a discrete representative set of values of mixture fraction, mixture fraction variance and the stoichiometric scalar dissipation rate and the results are stored in three-dimensional tables. Similarly, the mean values of temperature and density are calculated for the same discrete set of parameters plus one additional parameter, mean enthalpy gain/loss$\tilde{H}$. The results are stored in four-dimensional tables. During the flame simulation, the mean values of these quantities are obtained from interpolation of the stored data, rather than by explicit evaluation of the integrals.

4.2. *Mesh description and boundary conditions*

Due to the symmetry of the burner, a geometrically axisymmetric computational model is constructed. The computational domain covers an area from 0 to 1 m in the axial direction and 0–0.0775 m in the radial direction. Totally 120(x) × 80(r) non-uniform grids are used in the simulations

Table 3 – Flame Froude numbers and flame lengths at different pressure.

P [atm]	1	5	10
Fr_f	5.38	5.33	5.32
L_f [m]	0.8	0.8	0.8

Table 4 – Flame half widths, $r_{1/2}$ [m] at different pressure.

P [atm]	1	5	10
$x/D_J = 23$	0.00714	0.0064	0.0061
$x/D_J = 90$	0.0274	0.0258	0.025

with finer grids placed in the primary reaction zone, near the fuel nozzle exit region and near the wall. The numerical accuracy was checked by comparing the predicted results corresponding to the grid mentioned above with that obtained using a finer grid with 180 nodes in the axial direction and 120 nodes in the radial direction. It was found that the two sets of results are very close to each other and therefore may be regarded as grid independent.

The inflow boundary conditions including the inflow velocity profile and the turbulence intensity level are adopted from published experimental work of Barlow and Carter [16]. At the outlet region, outflow condition is assumed.

4.3. *Numerical methodology*

The governing equations described above are solved numerically in axisymmetric cylindrical coordinates using the commercial software Fluent, version 6.3. An implicit solution based on finite volume method in axisymmetric cylindrical coordinates is used. The SIMPLE numerical scheme is applied to handle the pressure and velocity coupling. The convective and the diffusion terms in the conservation equations are, respectively, discretized using the second-order upwind and the second-order central approximation of the corresponding fluxes at the cell faces. The governing equation of momentum, mixture fraction and its variance and energy are solved in a fully coupled fashion at each control volume.

5. Results and discussion

5.1. *Numerical model validation*

The model accuracy has been assessed in this flame configuration at atmospheric pressure in previous study [17]. It was shown that the flow field and mixing are sufficiently well described. In addition, heat losses due to radiation are found to be modelled satisfactorily since the maximum flame temperatures are predicted well. However, the spreading rate of the flame was slightly underpredicted and the flame length therefore slightly overpredicted.

Further validation of the model was conducted at high pressure. The recent high pressure, underexpanded hydrogen jet flame experiment of Schefer et al. [11] provides important data for model validation. The experiment consisted of a blowdown from a tank connected to a stagnation chamber just upstream of the 5.08 mm diameter jet opening. During the blowdown which lasted about 10 min, the stagnation pressure and jet flame length gradually decreased. For model validation, a time of 100 s into the blowdown was selected when the stagnation pressure and temperature upstream of the jet opening were 104.8 bar and 231.4 K, respectively. At these conditions, the flame visible length, $l_{visible}$, was 670 cm. Simulations used Mach Disk approach to model the underexpanded jet region as reported in Ref. [10]. Fig. 2 shows a comparison between predictions and experiments in the case of centerline temperature. Reasonable agreement is obtained at this flame conditions.

5.2. *Numerical results*

Hereafter, computational predictions are analysed at two flame heights. The first one ($x/D_J = 23$) represent the near-field region of the flames and the second one ($x/D_J = 90$) the far-field region.

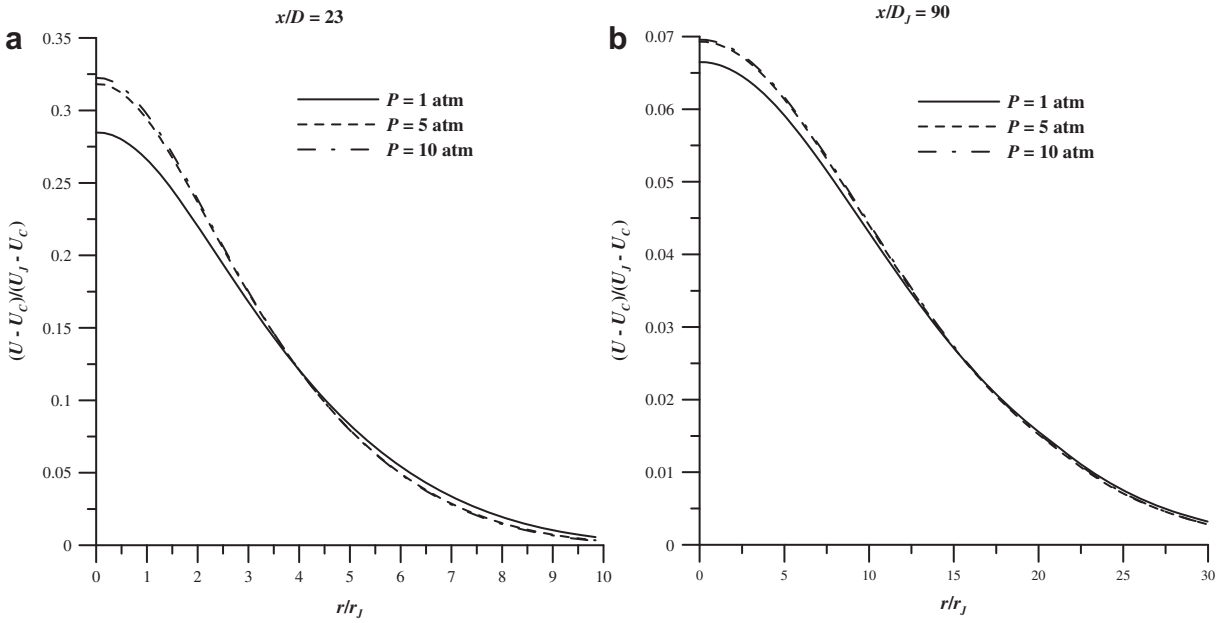

Fig. 4 – Radial profiles of normalized mean longitudinal velocity.

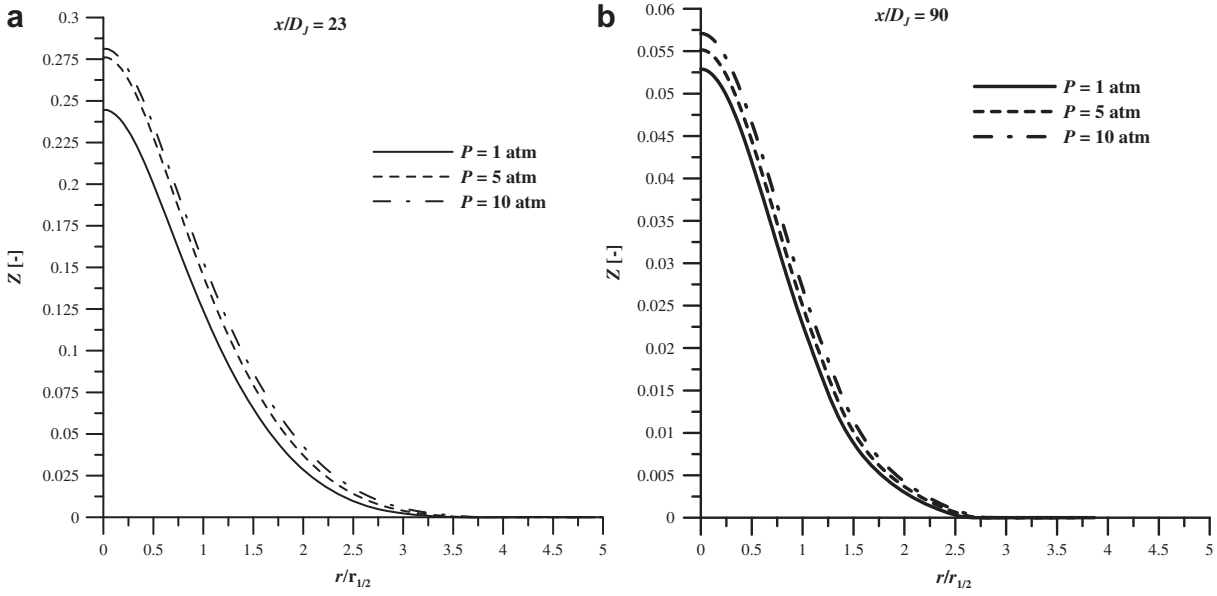

Fig. 5 – Radial profiles of mixture fraction.

The flame characteristics are determined over a range of operating pressure (Table 2). The numerical experiments are carried out keeping constant the volumetric flow rate of fuel and air. Under these conditions, only the fuel jet Reynolds number varies. In Table 2, *MR* is the momentum ratio between fuel and air jets. It is defined as [31]:

$$MR = \frac{\rho_J U_J^2}{\rho_c U_c^2} \tag{15}$$

5.2.1. *Pressure effect on flame length and width*

Fist of all, the flames length and width are evaluated in the range of operating pressure considered. The primary factor which affect the turbulent flame length are (i) Froude number, Fr_f, (ii) the stoichiometric mixture fraction, Z_{st}, (iii) air/fuel density ratio, ρ_J/ρ_c, (iv) the effective diameter of the burner, D_J, and the adiabatic flame temperature, T_f. A global flame Froude number can be defined based on the analysis presented by Delichatsios [32] and Bahadori et al. [33]:

$$Fr_f = \frac{U_J Z_{st}^{1.5}}{\left(\frac{\rho_J}{\rho_c}\right)^{0.25}\left(\frac{T_f - T_c}{T_c} g D_J\right)^{0.5}} \tag{16}$$

Delichatsios [33] proposed a general expression for non-dimensional flame length:

$$L^* = \frac{L_f Z_{st}}{D_J\left(\frac{\rho_J}{\rho_c}\right)^{0.2}} \tag{17}$$

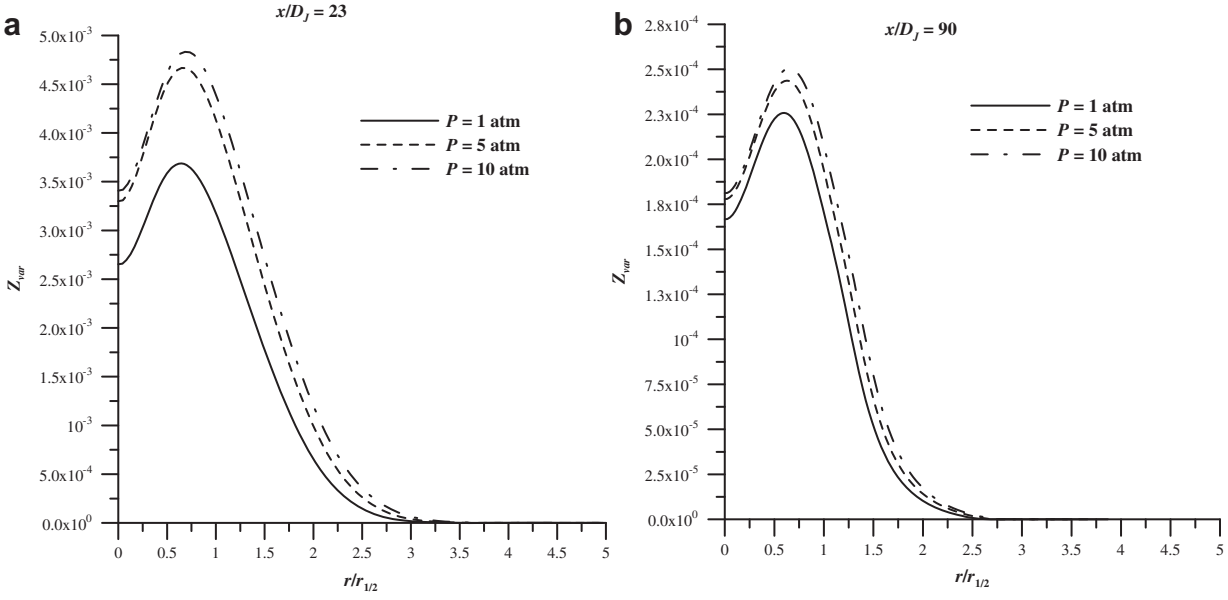

Fig. 6 – Radial profiles of mixture fraction variance.

In the buoyancy-dominated regime, L^* is correlated by the expression:

$$L^* = \frac{13.5Fr_f^{0.4}}{\left(1+0.07Fr_f^2\right)^{0.2}} \quad \text{for} \quad Fr_f < 5 \tag{18}$$

and for momentum-dominated regime by the expression:

$$L^* = 23 \quad \text{for} \quad Fr_f \geq 5 \tag{19}$$

Recent results by Schefer et *al.* [11] showed that this correlation works well for vertical turbulent hydrogen jets, both subsonic and choked, originating from sources at pressures up to 172 bar.

The adiabatic flame temperature in Eq. (16) is obtained from the thermodynamic equilibrium calculation. From Fig. 3, the adiabatic flame temperature increases rapidly from 1 to 5 atm and more gradually from 5 to 10 atm.

Values of flame Froude number and flame length (L_f) over the range of operating pressure considered are given in Table 3. The data collapse well onto the momentum-dominated correlation Eq. (19). Pressure has no effect on flame length as flame Froude number values are always higher than 5.

To quantify the jet flame spreading rate due to the turbulent mixing between the central jet and the co-flow air, the jet half-velocity width is analysed. From Table 4, the jet half width decreases with increasing pressure from 1 to 10 atm. At the first station, the jet half width is very sensitive to pressure whereas less dependency is noticed in the second location. The calculation of jet half width is directly linked to the radial expansion of mean longitudinal velocity [34]. The radial profiles of normalized mean longitudinal velocity, $(U - U_c)/(U_J - U_c)$, at two sections are shown in Fig. 4. This figure reveals on one hand that the radial expansion dependency to ambient pressure is noticeable in the near-field region whereas it is less far downstream, and on the other hand, that the radial decay rate decrease quickly between 1 and 5 atm and more slowly from 5 to 10 atm. Note that the flame half width, $r_{1/2}(x)$, is defined as the radius at which $(U - U_c) = 1/2(U_{center} - U_c)$ in order to take into account the co-flow effect [35]. The half width is used to normalize the radial coordinate in species and temperature profiles.

5.2.2. *Pressure effect on flame structure*

Before proceeding to a detailed analysis of predicted profiles, it is important to highlight the effect of pressure on mixing. Turbulent mixing is of great importance in turbulent non-premixed flames as chemical reactions occur only if fuel and oxidizer are mixed at the molecular level. Mixture fraction, its variance and the scalar dissipation rate are considered as an indicator of mixing quality. Mixture fraction characterizes the mixing state between fuel and oxidizer while the scalar fluctuation intensity reflects the effect of unmixedness. The scalar dissipation rate describes the local rate at which fine-scale mixing is occurring. It provides in addition a measure of the maximum possible chemical reaction rate which leads to nonequilibrium effects. Its modelling, in the SLFM approach, is based on proportionality of mechanical and scalar time scales [28].

Radial profiles of mixture fraction and its variance at two sections are plotted in Figs. 5 and 6. In these two locations, mixture fraction decays too slowly over the normalized flame radius whereas its corresponding fluctuations increase when pressure rise from 1 to 10 atm. Note that at $x/D_J = 90$ (Figs. 5 and 6b) mixture fraction and its variance profiles are less sensitive to pressure. Radial profiles of mean mixture fraction and its fluctuations reveal that the turbulent mixing layer has a very similar shape at different pressure considered. However, the pressure increases the width of the turbulent mixing layer and the level of fluctuations.

An analysis of the scalar dissipation rate field would provide information about fundamental processes of turbulent mixing. In Fig. 7, high values of the scalar dissipation rate

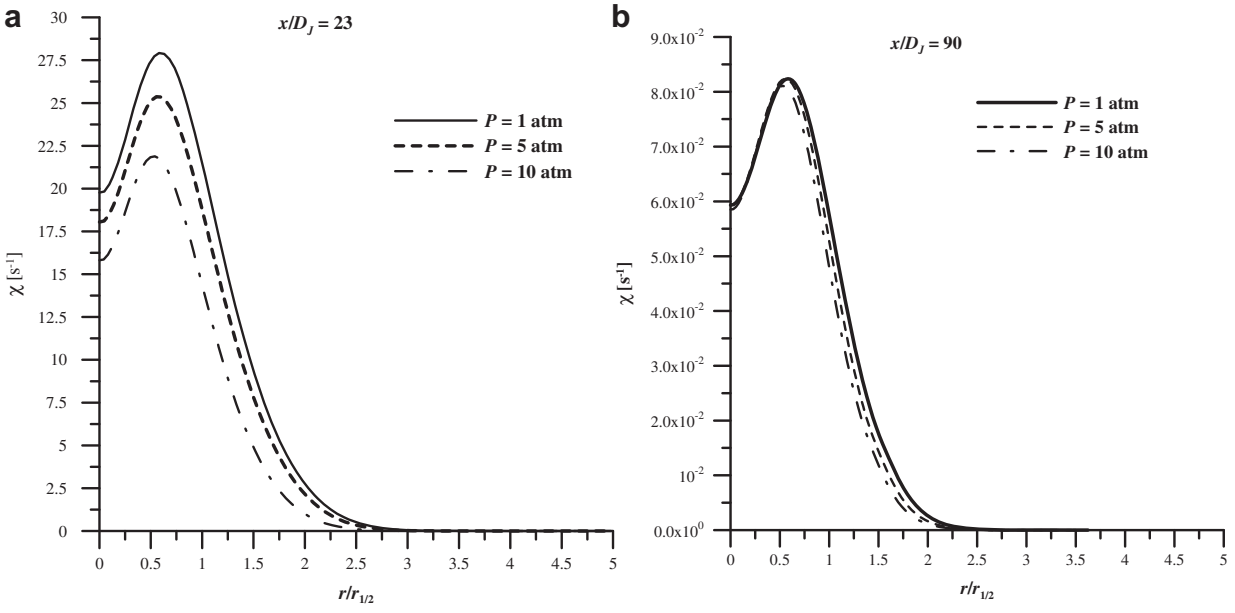

Fig. 7 – Radial profiles of the scalar dissipation rate.

are concentrated in the near-field region while low values exist in the far-field region. The scalar dissipation rate magnitudes decrease with pressure although the effect being less significant in the second location.

The predictions above of mixture fraction, its variance and the scalar dissipation rate revealed a deterioration of mixing with pressure rise.

The effect of pressure on the flame structure is illustrated at two axial positions in Figs. 8 and 9. According to these results, the following remarks can be underlined:

At $x/D_J = 23$ (Fig. 8), pressure rise induces a shift of the radial spreading profiles of the involved species and temperature towards the air side. This shift increases rapidly up to a pressure of 5 atm and more gradually at higher pressures. H_2 mass fraction increases (Fig. 8a) while O_2 mass fraction decreases (Fig. 8b) with pressure. A fast increase of the peak of H_2O (Fig. 8c) and temperature (Fig. 8d) is noticed from 1 to 5 atm (for example, 1.12% for water and 7% for temperature at $x/D_J = 23$), whereas slower increase can be seen from 5 to 10 atm (for example 0.75% for water and 2% for temperature at $x/D_J = 23$). More elaborate discussion on maximum flame temperature rise is presented later.

In the second location $x/D_J = 90$ (Fig. 9), the radial decay of the involved species and temperature profiles is less sensitive to operating pressure as in the first station. However, temperature and H_2O maximums still slightly increase with pressure.

Fig. 10 shows the variation of OH radical. OH is the major intermediate species in a H_2/air flame. The active OH radical concentration in the flame keeps decreasing with pressure.

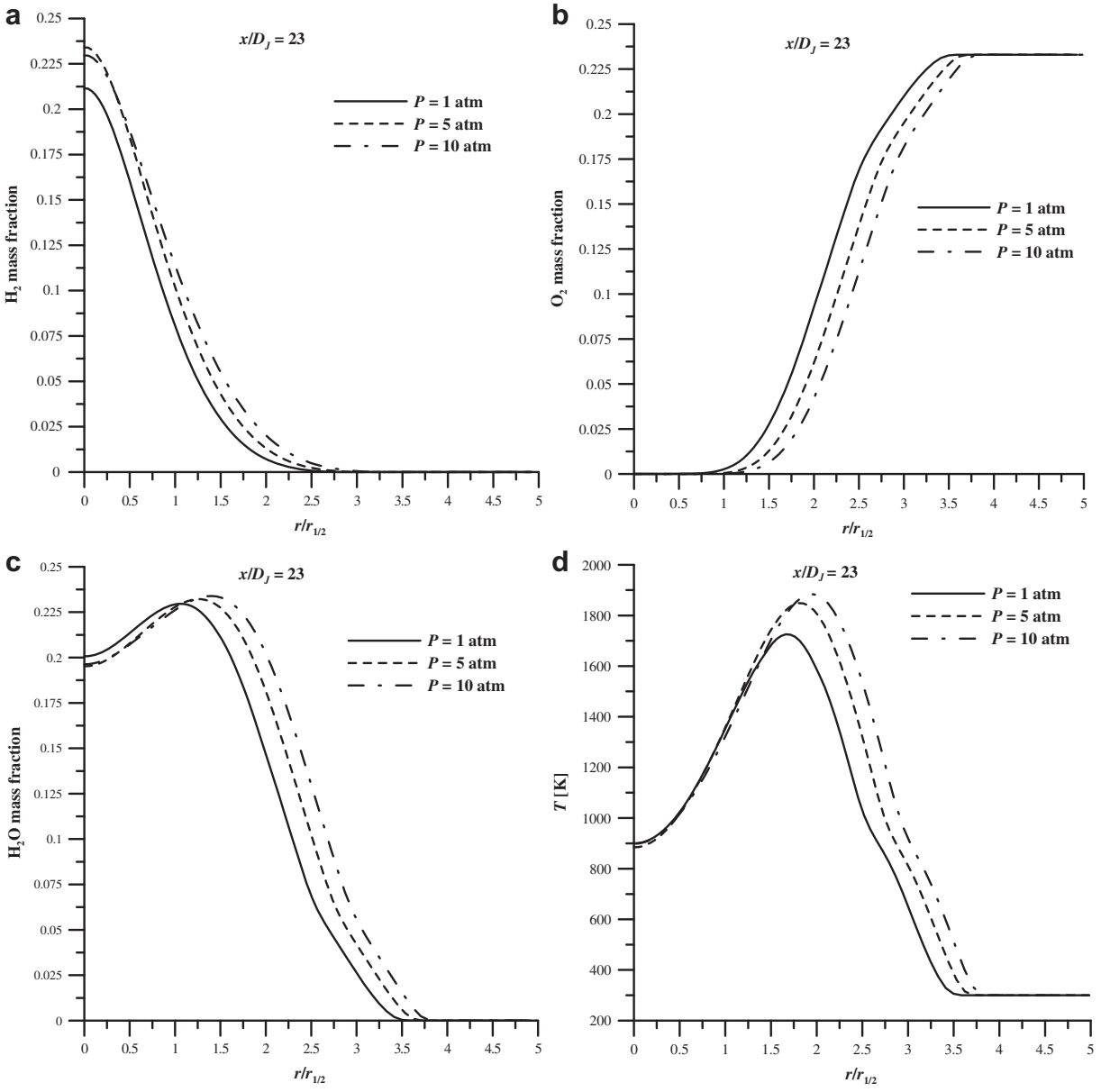

Fig. 8 – Effect of operating pressure on radial profiles, respectively, of (a) H_2 mass fraction (b) O_2 mass fraction (c) H_2O mass fraction and (d) temperature at $x/D_J = 23$.

The maximum value of this radical decreases by a factor of 63% as the pressure increases from 1 to 10 atm at $x/D_J = 23$ and 51% at $x/D_J = 90$. The significant effect of pressure on the concentration of OH radical is attributed to the recombination reactions involving a third body which are more favoured at higher pressures [36].

Below, flame fractional temperature [37] is introduced to characterize flame radiation:

$$\text{frac} = \frac{T_{\text{nonrad}} - T_{\text{rad}}}{T_{\text{nonrad}}} \tag{20}$$

In this equation, T_{rad} is the flame temperatures with the inclusion of radiative heat flux and T_{nonrad} is the flame temperatures without radiative heat flux.

The fractional flame temperature variation is only significant in the second section (Fig. 11) where it increases continuously with pressure. The effect of thermal radiation is thus important with low values of the scalar dissipation rate.

In the framework of SLFM approach, mixture fraction, its variance and the scalar dissipation rate are needed to deduce flame characteristics from flamelet library. The previous results indicated that the trends of these parameters depend on operating pressure which may cause some differences between the corresponding species mass fraction and temperature profiles. Species mass fraction and temperature profiles (Figs. 8 and 9) exhibit the same trend as mixture fraction. On the other hand at $x/D_J = 23$, the peak flame temperature increase is mainly related to the decrease of the scalar dissipation rate and the absence of flame radiation. Further downstream at $x/D_J = 90$, however, the scalar dissipation rate decrease balance almost the heat losses by

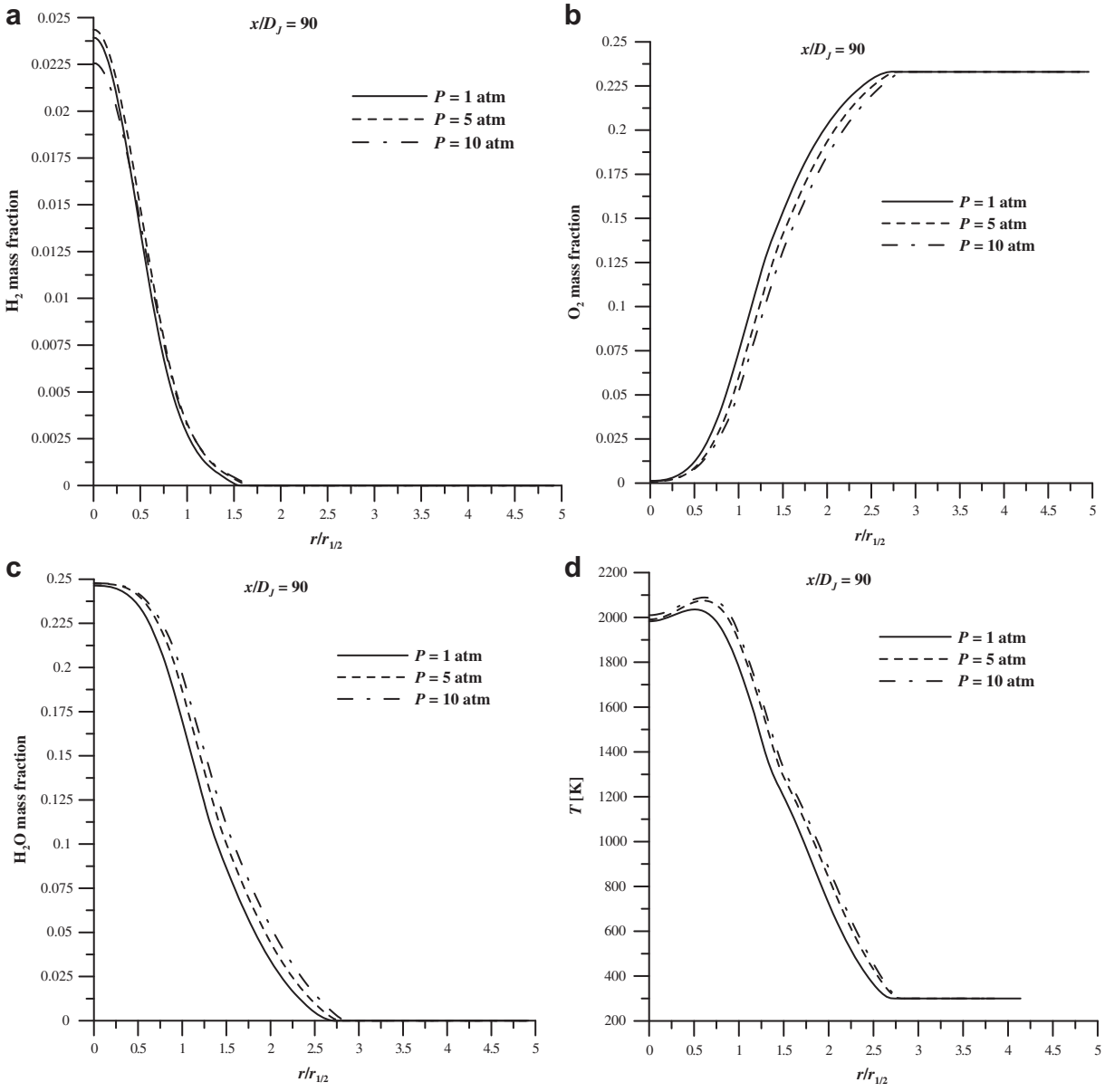

Fig. 9 – Effect of operating pressure on radial profiles, respectively, of (a) H_2 mass fraction (b) O_2 mass fraction (c) H_2O mass fraction and (d) temperature at $x/D_J = 90$.

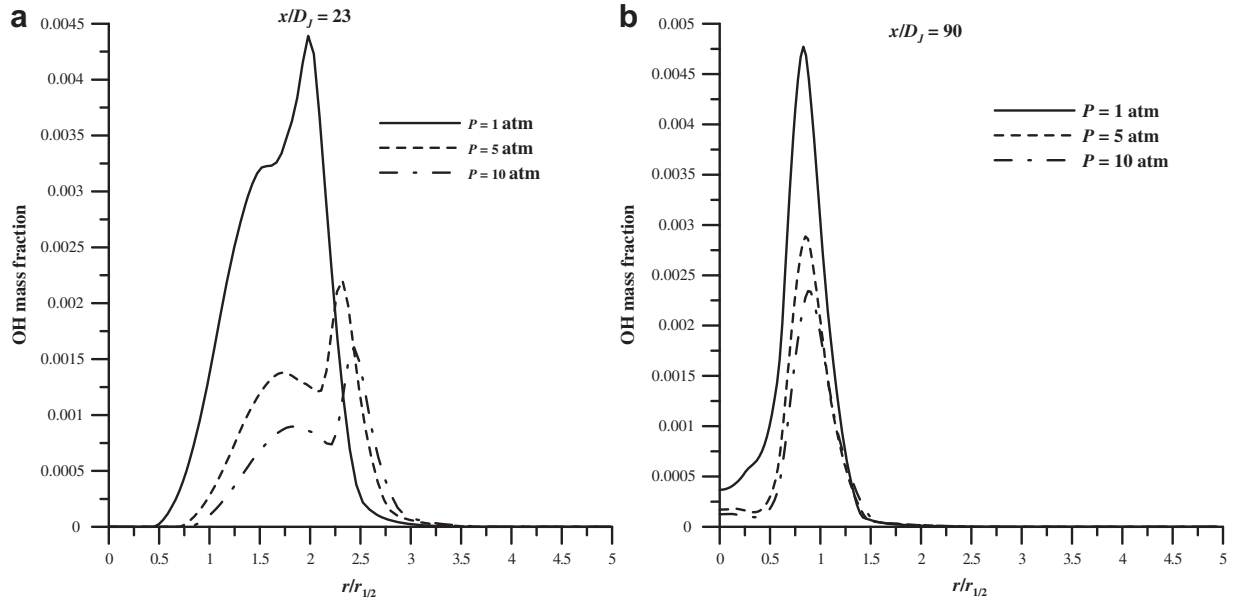

Fig. 10 – Radial profiles of OH mass fraction.

radiation. This temperature behaviour is consistent with the observations of [37] in the case of methane-air flames.

The results presented above indicate that pressure has a negative impact on mixing. Such influence is reasoned hereafter by examining the axial evolution of two parameters which are mean velocity and turbulent kinetic energy respectively.

Fig. 12 presents the axial evolution, as a function of the downstream distance x/D_J, of the mean velocity U for the three operating pressures using the usual dimensionless presentation $(U_J - U_c)/(U - U_c)$. The centerline velocity decay rates are strongly affected by pressure. Increasing pressure causes a rapid decrease of the decay rate of the axial velocity.

Dimensionless axial profiles of turbulent kinetic energy as a function of the downstream distance x/D_J are depicted in Fig. 13. From the fuel exit section, and moving downstream, a rapid increase of the kinetic energy is observed reaching an asymptotic level then decreases gradually. The axial position of turbulent kinetic energy maximum moves downstream of the jet exit section with pressure increases. The value of this maximum depends on the operating pressure which decreases with pressure increase.

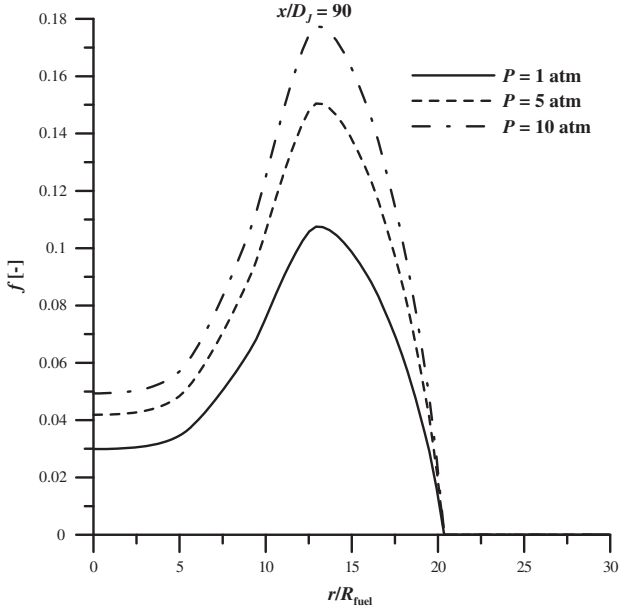

Fig. 11 – Radial profiles of flame fractional temperature.

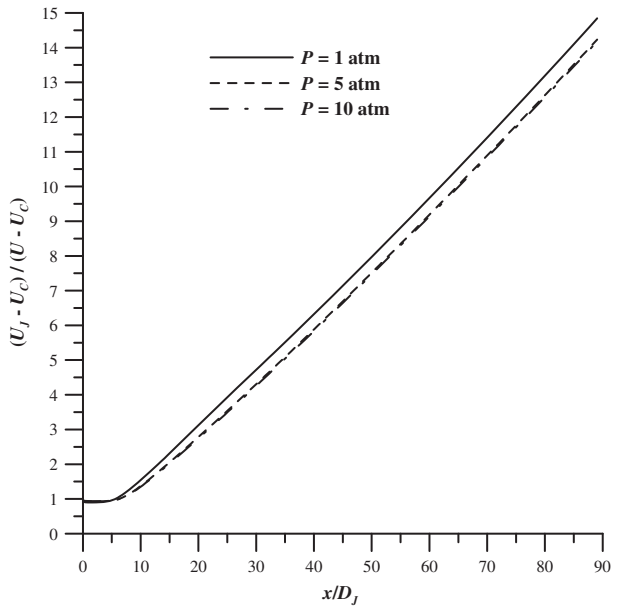

Fig. 12 – Axial profiles of dimensionless mean velocity.

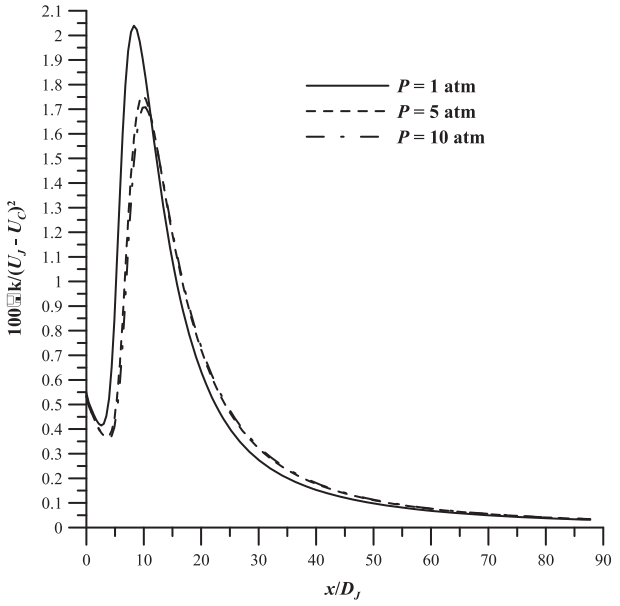

Fig. 13 – Axial profiles of dimensionless turbulent kinetic energy.

Mixing is most effective when the decay rate of the axial velocity increase together with the kinetic energy maximum. Accordingly, the gas becomes increasingly heavy with pressure rise, which hampered its ability to blend. This is related to the density of the jet which increases with pressure (Table 2) [34]. Light gases tend to mix more quickly with the ambient one than heavy gases. These observations are consistent with the behaviour of variable-density turbulent jets [34].

6. Conclusion

This study addressed the influence of elevated pressures up to 10 atm on turbulent non-premixed H_2/air flame structure and particular attention has been paid to mixing. The investigations were conducted at constant total volumetric fuel and air flows. The simulations included coupled models for turbulence, combustion and radiation. Turbulence was modelled with the k-ε closure. The flamelet library approach was applied to account for chemistry and turbulence interactions. Experimental data for hydrogen jet flames at atmospheric and higher pressures were used for model validation.

The computational results showed significant effects of pressure on mixing, radiation and flame structure, indicating an overall deterioration of mixing and an increase of radiation. It was observed that flame reaction zone became thicker as pressure increase. A relatively noticeable fast increase of the peak of temperature and H_2O was noticed from 1 to 5 atm where it is less for the range between 5 and 10 atm. The concentration of important intermediate radicals OH was found to decrease considerably with pressure.

REFERENCES

[1] Cormos CC. Evaluation of energy integration aspects for IGCC-based hydrogen and electricity co-production with carbon capture and storage. Int J Hydrogen Energy 2010;35:7485–97.
[2] Speth RL. Fundamental studies in hydrogen-rich combustion: Instability mechanisms and dynamic mode selection. PhD thesis, Massachusetts Inst Technology USA, 2010.
[3] Gobbato P, Masi M, Toffolo A, Lazzaretto A. Numerical simulation of a hydrogen fuelled gas turbine combustor. Int J Hydrogen Energy 2011;36:7993–8002.
[4] Weiland NT, Strakey PA. NO_x Reduction by Air-Side vs. Fuel-Side Dilution in Hydrogen Diffusion Flame Combustors. P. ASME Turbo Expo GT2009-877; 2009.
[5] Bouvet N, Chauveau C, Gökalp I, Lee SY, Santoro RJ. Characterization of syngas laminar flames using the bunsen burner configuration. Int J Hydrogen Energy 2011;36:992–1005.
[6] Shih H-Y. Computed extinction limits and flame structures of H_2/O_2 counterflow diffusion flames with CO_2 dilution. Int J Hydrogen Energy 2009;34:4005–13.
[7] Ribert G, Zong N, Yang V, Pons L, Darabiha N, Candel S. Counterflow diffusion flames of general fluids: oxygen/hydrogen mixtures. Combust Flame 2008;154:319–30.
[8] Gutheil E, Williams FA. A numerical and asymptotic investigation of structures of hydrogen–air diffusion flames at pressures and temperatures of high-speed combustion, 23. Proceedings of the Combustion Institute 1991;. 513–521.
[9] Sohn CH, Chung SH, Lee SR, Kim JS. Structure and acoustic pressure response of hydrogen–oxygen diffusion flames at high pressure. Combust Flame 1998;115:299–312.
[10] Houf WG, Evans GH, Schefer RW. Analysis of jet flames and unignited jets from unintended releases of hydrogen. Int J Hydrogen Energy 2009;34:5961–9.
[11] Schefer RW, Houfa WG, Williams TC, Bourneb B, Coltonb J. Characterization of high-pressure, underexpanded hydrogen-jet flames. Int J Hydrogen Energy 2007;32:2081–93.
[12] Schefer RW, Houfa WG, Bourneb B, Coltonb J. Spatial and radiative properties of an open-flame hydrogen plume. Int J Hydrogen Energy 2006;31:1332–40.
[13] Zheng J, et al. Numerical simulation of high-pressure hydrogen jet flames during bonfire test, Int J Hydrogen Energy, in press.
[14] Ghenai Chaouki. Combustion of syngas fuel in gas turbine can combustor. Adv Mech Eng 2010;2010:13. doi:10.1155/2010/342357. Article ID 342357.
[15] Chiesa P, Lozza G, Mazzocchi L. Using hydrogen as gas turbine fuel. J Eng for Gas Turbine Power 2005;127:73–80.
[16] Barlow RS, Carter CD. Raman/Rayleigh/LIF measurements of Nitric Oxide formation in turbulent hydrogen jet flames. Combust Flame 1994;3-4(97):261–80.
[17] Tabet-Helal F, Sarh B, Menou A, Gökalp I. A comparative study of turbulence modelling in hydrogen air nonpremixed turbulent flames. Combust Sci Technol 2006;178:1887–906.
[18] http://www.sandia.gov/TNF/DataArch/H2HeData.html.
[19] Flury M, Schlatter M. Influence of seeding methods on LDV measurements. Proc Combust Inst 1996;26. Work in progress.
[20] Pope SB. An explanation of the round jet/plane jet Anomaly. AIAA J 1978;16(3):279–81.
[21] Pitsch H, Peters NA. Consistent flamelet formulation for non-premixed combustion considering differential diffusion effects. Combust Flame 1998;114:26–40.
[22] Peters N. Turbulent combustion. Cambridge University Press; 2000.
[23] Yetter RA, Dryer FL, Rabitz H. A comprehensive reaction mechanism for carbon monoxide / hydrogen / oxygen kinetics. Combust Sci Technol 1991;79:97–128.

[24] Cavalierea DE, de Joannonb M, Sabiab P, Sirignanoa M, D'Annaa A. A comprehensive kinetic modeling of ignition of syngas-air mixtures at low temperatures and high pressures. Combust Sci Technol 2010;182:692–701.
[25] Kee RJ, Rupley FM, Miller JA, Coltrin ME, Grcar JF, Meeks E, et al. Chemkin collection, release 3.7.1. San Diego, CA: Reaction Design, Inc.; 2003.
[26] Binninger B, Chan M, Paczkko G, Hermann M. Numerical simulation of turbulent partially premixed hydrogen flames with the flamelet model; 1998. Technical Report, Advanced Combustion Gmbh, Internal Report.
[27] Coelho PJ, Teerling OJ, Roekaerts D. Spectral radiative effects and turbulence/radiation interaction in a non-luminous turbulent jet diffusion flame. Combust Flame 2003;133: 75–91.
[28] Jones WP, Whitelaw JH. Calculation methods for reacting turbulent flows. Combust Flame 1982;48:1–26.
[29] Modest MF. Radiative heat transfer, mechanical and technical engineering. 2nd ed. New York: Academic Press; 2003.
[30] Barlow RS, Smith NSA, Chen JY, Bilger RW. Nitric Oxide formation in Dilute hydrogen jet flames: isolation of the effects of radiation and turbulence-chemistry submodels. Combust Flame 1999;117:4–31.
[31] Mahesh S, Mishra DP. Flame structure of LPG-air inverse diffusion flame in a backstep burner. Fuel 2010;89:2145–8.
[32] Delichatsios MA. Transition from momentum to buoyancy-controlled turbulent diffusion jet flames and flame height relationship. Combust Flame 1993;92:349–64.
[33] Bahadori MY, Stocker DP, Vaughan DF, Zhou L, Edelman RB. Effects of buoyancy on laminar, transitional and turbulent gas jet diffusion flames. Modern developments in energy, combustion and spectroscopy. New York: Pergamon Press; 1993.
[34] Amielh M, Djeridane T, Anselmet F, Fulachier L. Velocity near-field of variable density turbulent jets. Int J Heat Mass Transfer 1996;39:2149–64.
[35] Wang P, Fröhlich J, Michelassi V, Rodi W. Large-eddy simulation of variable-density turbulent axisymmetric jets. Int J Heat Fluid Flow 2008;29:654–64.
[36] Liu F, Thomson KA, Hongsheng G, Smallwood GJ. Numerical and experimental study of an axisymmetric coflow laminar methane–air diffusion flame at pressures between 5 and 40 atmospheres. Combust Flame 2006;146:456–71.
[37] Parka J, Bae DS, Cha MS, Yun JH, Keel SI, Cho HC, et al. Flame characteristics in H_2/CO synthetic gas diffusion flames diluted with CO_2: effects of radiative heat loss and mixture composition. Int J Hydrogen Energy 2008;33:7256–64.